# Multicarrier Multiplexing Continuous-Variable Quantum Key Distribution at Terahertz Bands Under Indoor Environment and in Inter-Satellite Links Communication

Chengji Liu , Changhua Zhu , *Member, IEEE*, Xiao Liu, Min Nie, Hong Yang, and Changxing Pei

*Abstract*—We propose a continuous-variable quantum key distribution (CVQKD) scheme at terahertz (THz) bands based on multicarrier multiplexing (MCM) technology. In this scheme, multiple Gaussian modulated subcarriers are coupled to transmit multipath superposed thermal Gaussian states. At the receiver, optical discrete Fourier transform (ODFT) is used to demultiplex the received subcarriers, and the keys can be generated in parallel by homodyne detection and post processing. We analyze the security of the scheme against the optimal collective Gaussian attack under indoor environment and in inter-satellite links respectively. Results indicate that by using MCM technology, each subchannel may be affected by crosstalk, resulting in slight shortening of the maximal transmission distance while the total secret key rate can be greatly increased. We also verify the feasibility of higher key rate and longer distance THz-QKD by using MCM technology in inter-satellite links communication. We expect this work will provide an efficient path to build a global quantum communication network.

*Index Terms*—Multicarrier multiplexing, continuous variable, quantum key distribution, terahertz, optical discrete Fourier transform.

Chengji Liu, Xiao Liu, and Changxing Pei are with the State Key Laboratory of Integrated Services Networks, Xidian University, Xi'an 710071, China (e-mail: liuchengjixidian@163.com; aixigogo@163.com; chxpei@xidian.edu.cn).

Changhua Zhu is with the State Key Laboratory of Integrated Services Networks, Xidian University, Xi'an 710071, China, with the Collaborative Innovation Center of Quantum Information of Shaanxi Province, Xidian University, Xi'an 710071, China, and also with the Shaanxi Key Laboratory of Information Communication Network and Security, Xi'an University of Posts & Telecommunications, Xi'an 710121, China (e-mail: chhzhu@xidian.edu.cn).

Min Nie is with the Shaanxi Key Laboratory of Information Communication Network and Security, Xi'an University of Posts & Telecommunications, Xi'an 710121, China, and also with the School of Communications and Information Engineering, Xi'an University of Posts & Telecommunications, Xi'an 710121, China (e-mail: niemin@xupt.edu.cn).

Hong Yang is with the State Key Laboratory of Integrated Services Networks, Xidian University, Xi'an 710071, China, and also with the Institute of Spacecraft System Engineering, China Academy of Space Technology, Beijing 100094, China (e-mail: 13381105509@189.cn).

Digital Object Identifier 10.1109/JPHOT.2021.3098717

## I. INTRODUCTION

CONTINUOUS-variable quantum key distribution (CVQKD) allows two participants, Alice (the sender) and Bob (the receiver), to share common secret keys over an untrusted environment [1]–[8]. Compared with discrete-variable quantum key distribution (DVQKD) [9], [10], CVQKD does not require single photon detectors and can be integrated easily with classical optical communication systems [5], [11]–[25]. The existing QKD systems mostly use photons to carry information and transmit them through optical fiber or free-space channels. However, with the rapid development of wireless communications, information security and scarcity of spectrum resources are becoming more and more serious. Terahertz (THz) communication systems are expected to become increasingly important in modern applications, e.g., high-speed short-range wireless communications [26]–[31] and satellite communications [32]–[34]. Moreover, compared with free-space optical links, the performance of THz wireless links has almost no degradation in the presence of atmospheric turbulence, fog, and dust, etc. While, it has demonstrated that there are security risks in THz wireless links [35]. So, the exploration of QKD technology in the THz bands provides a feasible solution.

The communications at THz frequencies (0.1 THz-10 THz), combine the characteristics of microwave communications and optical communications. Compared with the former, THz communications possess large capacity, directionality and noise immunity; and compared with the latter, they has higher energy efficiency. The distance limitation of THz communications is mainly caused by the absorption of high water concentration in the atmosphere [36], [37]. However, noted that if the atmosphere is dry enough, then long-distance satellite-to-ground station communications can be carried out at THz frequencies. Antarctic-based ground station is a well-known example of the feasibility of such communications [34]. Fortunately, THz communications in inter-satellite links are completely feasible [32], because the concentration of water in the vacuum is negligible, and the advantages of THz communications can be fully utilized.

In fact, the feasibility of QKD systems at various wavelengths of the electromagnetic spectrum has been investigated in room temperature, and it also summaries the factors
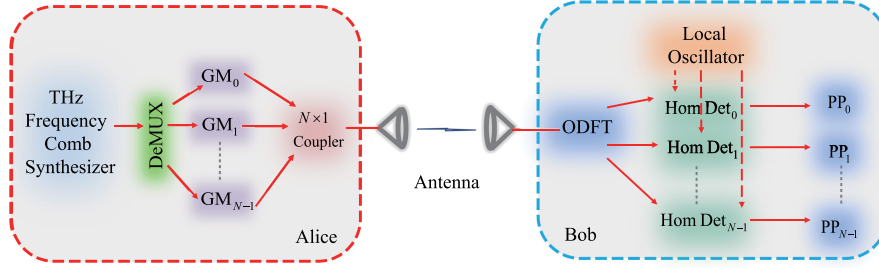
Fig. 1.    Structure diagram of THz-MCM-CVQKD system. DeMUX: demultiplexer; GM: $q/p$-Gaussian modulation; ODFT: optical discrete Fourier transform; HomDet: homodyne detection; PP: post processing.

affecting security [5]. In 2018, Ottaviani *et al.* [26] showed that CVQKD can operate at THz bands and derive the relevant secret key rate (SKR) against the optimal collective Gaussian attack. Liu *et al.* [27] discussed the feasibility of THz-CVQKD using thermal Gaussian states and provide a practical system under indoor environment. In 2019, Wang *et al.* [32] analyzed the feasibility of using THz bands as a means to achieve CVQKD in a Low-Earth-Orbit micro-satellites constellation.

Despite the noise characteristic of a THz-CVQKD system is credible and well usable in security proofs, the currently available SKR of the system need to be increased, which is consistent with the traditional fiber-based QKD. There are three possible methods to solve this problem. The first one is to design new protocols to increase the SKR. The second one is to improve the pulse repetition rate which requires higher work performance of detectors and postprocessing speed.

The third idea is to use multicarrier multiplexing (MCM) technology to generate parallel keys in QKD. In recent years, QKD based on MCM technology has attracted significant attention due to its ability to provide higher SKR [38]–[49]. The basic idea of the CVQKD based on MCM technology is that MCM divides the high-speed data sequence into several low-speed sequences and modulates them on subcarriers to achieve parallel key distribution. In 2015, Bahrani *et al.* [48] propose two possible schemes to significantly improve the key generation rate by using multiplexing technique for DVQKD systems. In the first scheme, subcarriers are generated directly by an optical comb generator or laser sources [50], [51]. After modulating the subcarriers, an optical coupler merges them to generate MCM signals. In the second one, MCM signals are generated by the optical inverse discrete Fourier transform (OIDFT) circuit [52]. Both schemes are dependent on real-time optical discrete Fourier transform (ODFT) at receivers [53].

Inspired by the first scheme, we propose a CVQKD protocol at THz bands based on MCM technology (THz-MCM-CVQKD). The superposition of multipath Gaussian states is realized by MCM and Gaussian modulation (GM). At the receiver, the subcarriers of Gaussian states are separated by ODFT, and the keys are obtained in parallel by homodyne detection and post processing. We analyze the security of the proposed QKD protocol against the optimal collective Gaussian attack strategy at THz bands under indoor environment and in inter-satellite links respectively.

This paper is organized as follows. In Section II, we propose the system construction and protocol procedure of the THz-MCM-CVQKD. In Section III, we analyze the security of the proposed QKD. Section IV analyzes the SKR of the system under indoor environment and in inter-satellite links. Finally, in Section V we give our conclusions.

## II.    QKD BASED ON MCM AT THz BANDS

### A.    Schematic Setup of THz-MCM-CVQKD

The schematic setup of THz-MCM-CVQKD is shown in Fig. 1, and the following description assumes the use of $N$ Gaussian subchannels for the transmission of subcarriers. At Alice's station, a THz frequency comb synthesizer [54] and a demultiplexer generate $N$ subcarriers of thermal states, which have the same frequency interval and are orthogonal in the frequency-domain. Each subcarrier is modulated by a $q/p$-Gaussian modulator ($q/p$-GM) [6]. The structure of the $q/p$-GM is shown in Fig 2. It consists of a double Mach-Zehnder interferometer (MZI), i.e., an MZI is embedded in each arm. A coherent state $|\alpha\rangle$ and an assisted vacuum state $|0\rangle$ are propagated in the double MZI by a balanced beam-splitter (BS$_1$). In the upper arm of the double MZI, an auxiliary state $|0\rangle$ is added again. The state in the upper arm of MZI$_1$ is modulated by phase shift $+\varphi_1$, the state in the lower arm of MZI$_1$ is modulated by phase shift $-\varphi_1$. In the lower arm of the double MZI, phase shifts $+\varphi_2$ and $-\varphi_2$ are added in the upper and lower arms of MZI$_2$, respectively. One of the output of the MZI$_2$ is shifted by $\pi/2$ and then is propagated in BS$_2$ with one of the output of the MZI$_1$. Finally the state $|\alpha'\rangle = |\alpha(\cos\varphi_1 + j\cos\varphi_2)/2\rangle$ is obtained [6]. After $q/p$-GM, the $N$ modulated states are

$$|\alpha_i\rangle = |q_i + jp_i\rangle, i = 0, 1, \ldots, N-1, \qquad (1)$$

with quadrature components $q_i$ and $p_i$ that are realizations of two random variables $Q$ and $P$. The random variables $Q$ and $P$ obey the same zero-centered normal distribution $Q \backsim P \backsim N(0, V_{\text{mod}})$. The transmitter input signals at Alice's station whose dimensionless operator is derived by

$$\hat{a}_i = \hat{Q}_i + j\hat{P}_i, i = 0, 1, \ldots, N-1. \qquad (2)$$
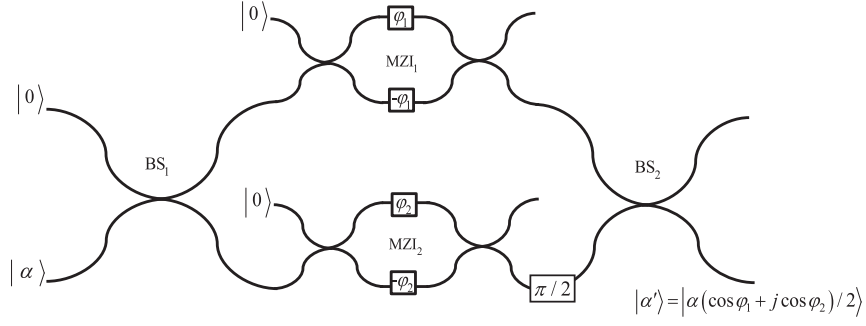
Fig. 2.  The schematic of a $q/p$ - Gaussian modulation.
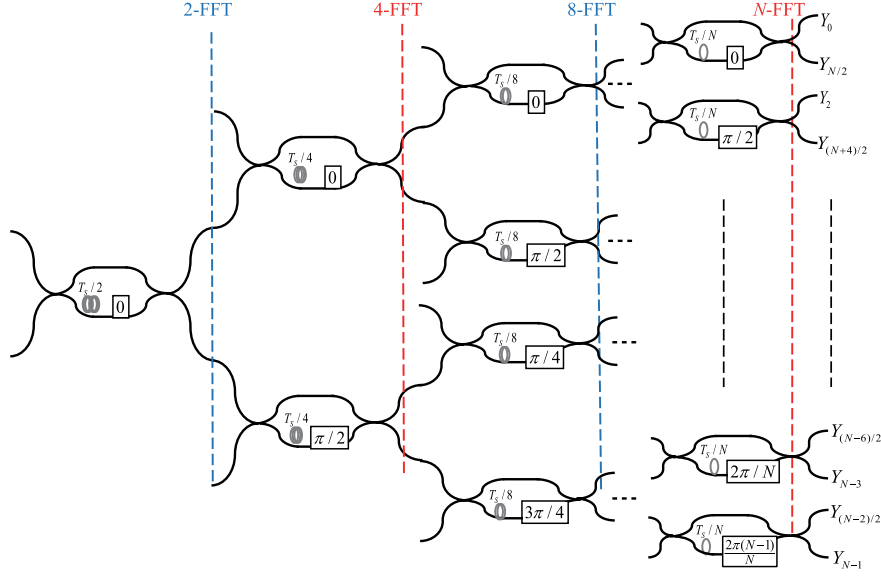


Fig. 3.  The $N$-way passive ODFT circuit.

The modulated quantum signals are combined by a $N \times 1$ coupler as

$$\hat{x}(t) = \sum_{i=0}^{N-1} \hat{a}_i e^{j2\pi f_i t}, \qquad (3)$$

where $f_i$ is the frequency of the $i$-th subcarrier.

After arriving at Bob's station, we ignore the influence of channel noise, which will be taken into account when we calculate the SKR. The received quantum signals can be given by

$$\hat{x}'(t) = \sum_{k=0}^{N-1} \hat{a}'_i e^{j2\pi f_i t}, 0 < t < T_s, \qquad (4)$$

where, $T_s$ is the pulse width. Then Bob decomposes them into $N$ subcarriers by performing ODFT operations. The implementation of ODFT is shown in Fig. 3 [50]. It is a passive structure composed of $N - 1$ MZIs. Through this structure, DFT can be achieved by phase shifting, coupling and delay, etc. Each output of the ODFT circuit is a weighted sum of shifted copies of the input. The output signals by performing ODFT operations are

as follows:

$$\hat{X}_m(t) = \sum_{n=0}^{N-1} \hat{x}'(t - nT_c) e^{\frac{-j2\pi nm}{N}}, \qquad (5)$$

where $T_c = T_s/N$. Substituting Eq. (4) into Eq. (5), we obtain

$$\hat{X}_m(t) = \sum_{k=0}^{N-1} \hat{a}'_i e^{j2\pi f_i t} \left( \sum_{n=0}^{N-1} e^{\frac{-j2\pi n(i+m)}{N}} e^{-j2\pi n f_0 T_c} \right), \qquad (6)$$

where $f_0$ is the initial frequency, $f_i = f_0 + i\Delta f$, and $\Delta f = 1/NT_c$ is the frequency interval of the subcarriers. Assuming $f_0$ and $T_c$ are constants. The term in brackets in Eq. (6) is nonzero only if $i + m = N$. Then we obtain

$$\hat{X}_m(t) = K_b \hat{a}'_{(N-m)} e^{j2\pi f_{(N-m)} t}, \qquad (7)$$

where $K_b$ is a constant and the $m$-th output corresponds to the frequency $f_{(N-m)}$.

Bob then sends $N$ output signals to $N$ homodyne detectors, $\text{HomDet}_0, \text{HomDet}_1, \ldots, \text{HomDet}_{N-1}$, respectively. The structure of the homodyne detection is shown in Fig. 4. The signal (Sig) and the local oscillator (LO) [6] are coherently mixed and then enter the detector. Finally, data acquisition and post-processing (PP) are performed.
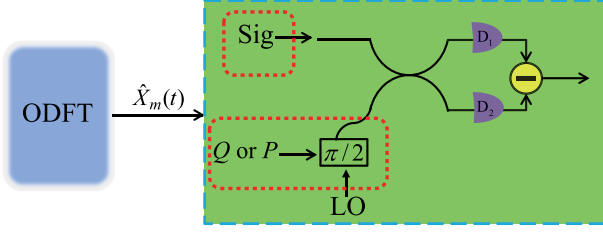
Fig. 4. The schematic of homodyne detection.

## B. Procedure of THz-MCM-CVQKD

In our protocol, Alice and Bob are two honest participants and we make the following assumptions for a THz-MCM-CVQKD:

1) Alice is the sender and is responsible for preparing for quantum signals.
2) Bob is the receiver, who resumes and detects the signals from Alice.
3) The classical channel is authenticated, while the quantum channel is insecure for eavesdropping.
4) The prepared noise is confined to Alice's station and unknown to eavesdropping.

There are four steps in the process of key distribution:

*Step 1 (Preparation):* Alice prepares $N$ THz subcarrier thermal states and performs $q/p$-Gaussian modulations $GM_0, GM_1, \ldots, GM_{N-1}$ on them respectively. After $q/p$-GM, she obtains $N$ modulated thermal states $|\alpha_i\rangle = |q_i + jp_i\rangle, i = 0, 1, \ldots, N-1$, with quadrature components $q_i$ and $p_i$ that are realizations of two random variables $Q$ and $P$. The random variables $Q$ and $P$ obey the same zero-centered normal distribution $Q \backsim P \backsim N(0, V_{\text{mod}})$. The $q/p$-GM variance is $V_{\text{mod}}$. The overall variance of the $i$-th quantum state prepared by Alice is $V_i = V_{A_i} = V_{\text{mod}_i} + V_S, i = 0, 1, \ldots, N-1$. Here $V_S$ is the shot noise. The relationship between $V_S$ and different frequencies is described by [5]

$$V_S = 2\bar{n} + 1, \qquad (8)$$

where $\bar{n}$ denotes the average photon number which is given by [5]

$$\bar{n} = \frac{1}{\exp(hf/\kappa\tau) - 1}, \qquad (9)$$

where $f$ is the frequency of quantum signals, $h$ is Planck's constant, $\kappa$ is Boltzmann's constant, and $\tau$ is the absolute temperature.

*Step 2 (Transmission):* Alice combines all modulated THz source subcarriers to generate quantum signals and then sends them to Bob.

*Step 3 (Detection):* After receiving the MCM pulses from Alice, Bob performs ODFT operation to decompose them into $N$ subcarriers. Then he sends the subcarriers to perform homodyne detection separately.

*Step 4 (Post-processing):* Bob samples the detection results and performs post-processing with Alice, including security check, information reconciliation and privacy amplification, and finally obtains the secret keys.

## III. SECURITY OF THz-MCM-CVQKD

### A. The Model of Noise and Eve's Attack

Apart from the specifications on signal modulation, a THz-MCM-CVQKD system can be characterized by the transmittance $T$ (channel transmission $T_{\text{ch}}$, detection efficiency $\eta$, etc.) and the noise $\xi$ (channel noise $\xi_{\text{ch}}$, detection noise $\xi_{\text{det}}$, etc.), in which the parameter of each subsystem is $(T_i, \xi_i), i = 0, 1, \ldots, N-1$. The subchannel noise can be given by [3]

$$\xi_{\text{ch}_i} = \frac{1 - T_{\text{ch}_i}}{T_{\text{ch}_i}} + \varepsilon_i, i = 0, 1, \ldots, N-1, \qquad (10)$$

where $\varepsilon_i$ is the excess noise (e.g., modulation noise, phase-recovery noise, Raman noise, etc.). Similarly, the dectection noise is represented as [3]

$$\xi_{\text{det}_i} = \frac{1 - \eta_i + v_{\text{el}}}{\eta_i}, i = 0, 1, \ldots, N-1, \qquad (11)$$

where $v_{\text{el}}$ is an additional variance caused by the electronic noise of the detector. The total noise of each subsystem is given by the sum:

$$\xi_i = \xi_{\text{ch}_i} + \frac{1}{T_{\text{ch}_i}}\xi_{\text{det}_i}. \qquad (12)$$

After transmitting the Alice's signal through the lossy and noisy channel, Bob will measure a total quadrature variance as [3]

$$V_{B_i} = T_{\text{ch}_i}\eta_i(V_i + \xi_i). \qquad (13)$$

Substituting Eq. (12) into Eq. (13), we obtain

$$
\begin{aligned}
V_{B_i} &= T_{\text{ch}_i}\eta_i \left( V_i + \xi_{\text{ch}_i} + \frac{1}{T_{\text{ch}_i}}\xi_{\text{det}} \right) \\
&= T_{\text{ch}_i}\eta_i \left( V_i + \frac{1 - T_{\text{ch}_i}}{T_{\text{ch}_i}} + \varepsilon_i + \frac{1}{T_{\text{ch}_i}} \left( \frac{1 - \eta_i + v_{el}}{\eta_i} \right) \right) \\
&= T_{\text{ch}_i}\eta_i V_i - T_{\text{ch}_i}\eta_i + T_{\text{ch}_i}\eta_i\varepsilon_i + 1 + v_{\text{el}} \\
&=: T_i(V_i - 1 + \sigma_i) + 1, \qquad (14)
\end{aligned}
$$

where we defined $T_i := T_{\text{ch}_i}\eta_i$, $\sigma_i := \varepsilon_i + v_{\text{el}}/T_i$.

In the channel communication, the optimal collective Gaussian attack is the most important type of Eve's attack [23], [24]. As is shown in Fig. 5, Eve prepares ancilla modes $\hat{E}'$ and $\hat{E}''$ in $N$ Einstein-Podolsky-Rosen (EPR) entangled Gaussian states $|\Psi\rangle^{\otimes N}$ with the variance of $W_i, i = 0, 1, \ldots, N-1$, respectively. One of the particle in each entangled pair interferes with the signal by a beam splitter with the transmittance $T_i$. Eve measures another particle of each entangled pair for obtaining useful imformation. This attack can be simply described by two parameters: the transmittance $T_i$ and the subchannel noise $W_i$. The latter parameter can be given by [5], [6]

$$W_i = 1 + \frac{T_i\sigma_i}{1 - T_i}, i = 0, 1, \ldots, N-1. \qquad (15)$$

Therefore, Eq. (14) can be reformulated as

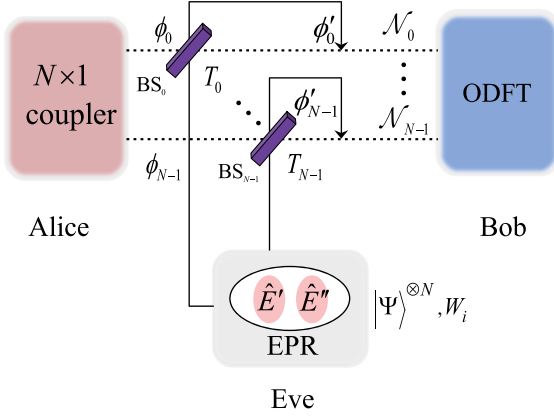$$V_{B_i} = (1 - T_i)W_i + T_iV_i. \qquad (16)$$

Fig. 5. Eve's attack model.

## B. Direct Reconciliation and Reverse Reconciliation

In the case of a single subcarrier, the key rate of the MCM system is consistent with the THz CVQKD protocol, therefore, the covariance matrix $\gamma_{AB_{(i)}}$ is denoted as [6]

$$\gamma_{AB_{(i)}} = \begin{pmatrix} V_i \cdot \mathbf{I} & \sqrt{T_i(V_i^2 - 1)} \cdot \mathbf{Z} \\ \sqrt{T_i(V_i^2 - 1)} \cdot \mathbf{Z} & [(1 - T_i)W_i + T_i V_i] \cdot \mathbf{I} \end{pmatrix} \tag{17}$$

Here, $\mathbf{I}$ and $\mathbf{Z}$ are the pauli matrices

$$\mathbf{I} = \begin{pmatrix} 1 & 0 \\ 0 & 1 \end{pmatrix}, \quad \mathbf{Z} = \begin{pmatrix} 1 & 0 \\ 0 & -1 \end{pmatrix}. \tag{18}$$

We begin the analysis of the SKR of THz-MCM-CVQKD system by considering direct reconciliation (denoted by the symbol ▶) using homodyne detection and then in the following section consider reverse reconciliation (denoted by the symbol ◀).

### A. Direct Reconciliation

The SKR $R_i^{\blacktriangleright}$ for direct reconciliation (DR) using homodyne detection is given by

$$R_i^{\blacktriangleright} = \beta I_{AB_{(i)}} - S_{AE_{(i)}}, \tag{19}$$

where $\beta$ is the reconciliation efficiency. $I_{AB_{(i)}}$ and $S_{AE_{(i)}}$ are the mutual information between Alice and Bob in the $i$-th subsystem and the amount of information stolen by Eve respectively.

The mutual information $I_{AB_{(i)}}$ using homodyne detection is given by [5], [6]

$$\begin{aligned} I_{AB_{(i)}}^{\text{hom}} &= \frac{1}{2}\log_2(1 + \text{SNR}_i) = \frac{1}{2}\log_2\left(\frac{V_{B_i}}{V_{B_i}|V_{A_i}}\right) \\ &= \frac{1}{2}\log_2\left[\frac{(1 - T_i)W_i + T_i V_i}{(1 - T_i)W_i + T_i V_S}\right], \end{aligned} \tag{20}$$

where, $\text{SNR}_i$ denotes the signal to noise ratio, which is the ratio between the total transmitted signal power and the total noise power in the $i$-th subsystem. The mutual information between Eve and Alice is bounded by the Holevo bound [5] $S_{AE_{(i)}}$ which is defined as,

$$S_{AE_{(i)}} = S_{E_i} - S_{(E|A)_i}, \tag{21}$$

where $S$ is the von Neumann entropy. For Gaussian states, the von Neumann entropy can be written by its symplectic eigenvalues

$$S = \sum_x h(x), \tag{22}$$

where

$$h(x) = \left(\frac{x + 1}{2}\right)\log_2\left(\frac{x + 1}{2}\right) - \left(\frac{x - 1}{2}\right)\log_2\left(\frac{x - 1}{2}\right). \tag{23}$$

To calculate von Neumann entropy of $S_{E_i}$ and $S_{(E|A)_i}$, we note that a two-mode covariance matrix in block form

$$\gamma = \begin{pmatrix} A & C \\ C^{\mathrm{T}} & B \end{pmatrix}. \tag{24}$$

The symplectic eigenvalues $v_1$ and $v_2$ of covariance matrix $\gamma$ can be calculated using the formula [5]

$$\nu = |i\Omega\gamma|, \tag{25}$$

where $v \geq 1$, the symbol $\Omega$ defines the symplectic form and is given by

$$\Omega := \bigoplus_{k=1}^{n} \begin{pmatrix} 0 & 1 \\ -1 & 0 \end{pmatrix}, \tag{26}$$

the symbol $\bigoplus$ is the direct sum indicating adding matrices on the block diagonal. The symplectic eigenvalues $v_1$ and $v_2$ can be written in the form

$$v_{1,2} = \sqrt{\frac{1}{2}(\Delta \pm \sqrt{\Delta^2 - 4\det\gamma})}, \tag{27}$$

where $\det\gamma$ is the determinant of the covariance matrix $\gamma$, $\Delta = \det A + \det B + 2\det C$ [4].

The covariance matrix corresponding to Eve's information of the $i$-th subsystem is

$$\gamma_{E_i} = \begin{pmatrix} ([1 - T_i]V_i + T_i W_i) \cdot \mathbf{I} & \sqrt{T_i(W_i^2 - 1)} \cdot \mathbf{Z} \\ \sqrt{T_i(W_i^2 - 1)} \cdot \mathbf{Z} & W_i \cdot \mathbf{I} \end{pmatrix}. \tag{28}$$

Therefore Eve's symplectic eigenvalues can be obtained by using Eq. (27).

Next we need to calculate symplectic eigenvalues of the covariance matrix $\gamma_{(E|A)_i}$. Eve's covariance matrix is made up from the two modes $\hat{E}'$ and $\hat{E}''$:

$$\gamma_E(V, V) = \begin{pmatrix} \text{diag}\,[m_V, m_V] & \varphi \cdot \mathbf{Z} \\ \varphi \cdot \mathbf{Z} & W_i \cdot \mathbf{I} \end{pmatrix}, \tag{29}$$

where $m_V = (1 - T_i)V + T_i W_i$, $\varphi = [T_i(W_i^2 - 1)]^{1/2}$ and the symbol "diag" represents a diagonal matrix. Eve's conditional covariance matrix is given by [5]

$$\gamma_{(E|A)_i} = \gamma_E(V_S, V_i) - (V_{A_i})^{-1}\mathbf{C}\Pi\mathbf{C}^{\mathrm{T}}, \tag{30}$$

where $V_{A_i} = V_i$,

$$\Pi := \begin{pmatrix} 1 & 0 \\ 0 & 0 \end{pmatrix}, \quad \mathbf{C} = \begin{pmatrix} -\sqrt{1 - T_i}\sqrt{V_i^2 - 1} \cdot \mathbf{Z} \\ 0 \end{pmatrix}. \tag{31}$$

We can conclude from Eq. (30) and Eq. (31) that

$$\gamma_{(E|A)_i} = \begin{pmatrix} D & E \\ E^{\mathrm{T}} & F \end{pmatrix}, \tag{32}$$

where

$$D = \begin{pmatrix} \frac{(1-T_i)(V_iV_S-V_i^2+1)}{V_i} + T_iW_i & 0 \\ 0 & (1-T_i)V_i + T_iW_i \end{pmatrix},$$

$$E = \sqrt{T_i\left(W_i^2 - 1\right)} \cdot \mathbf{Z},$$

$$F = W_i \cdot \mathbf{I}. \tag{33}$$

Using Eq. (27), the corresponding symplectic eigenvalues of $\gamma_{(E|A)_i}$ can be calculated, thereby we can obtain the SKR $R_i^\blacktriangleright$ for DR using homodyne detection.

*B. Reverse Reconciliation*

The SKR $R_i^\blacktriangleleft$ for reverse reconciliation (RR) using homodyne detection is given by

$$R_i^\blacktriangleleft = \beta I_{AB_{(i)}} - S_{BE_{(i)}}, \tag{34}$$

where $I_{AB_{(i)}}$ is defined in Eq. (20). The Holevo bound between Eve and Bob $S_{BE_{(i)}}$ is defined as,

$$S_{BE_{(i)}} = S_{E_i} - S_{(E|B)_i}. \tag{35}$$

For RR, $S_{BE_{(i)}}$ can be simplified as [6]

$$S_{BE_{(i)}} = S_{E_i} - S_{(E|B)_i} \quad = S_{AB_{(i)}} - S_{(A|B)_i}. \tag{36}$$

The covariance matrix $\gamma_{AB_{(i)}}$ corresponding to Alice's and Bob's information of the $i$-th subsystem is defined in Eq. (17). We can simplify $\gamma_{AB_{(i)}}$ to the following form,

$$\gamma_{AB_{(i)}} = \begin{pmatrix} a \cdot \mathbf{I} & c \cdot \mathbf{Z} \\ c \cdot \mathbf{Z} & b \cdot \mathbf{I} \end{pmatrix}. \tag{37}$$

Using Eq. (25), the symplectic eigenvalues $v_{1,2}$ of $\gamma_{AB_{(i)}}$ is given by

$$v_{1,2} = \frac{1}{2}(z \pm [b - a]), \tag{38}$$

where $z = \sqrt{(a+b)^2 - 4c^2}$. These two eigenvalues can be used to calculate the entropy $S_{AB_{(i)}}$. The derivation method of the covariance matrix $\gamma_{(A|B)_i}$ is the same as Eq. (30), which is given by

$$\gamma_{(A|B)_i} = \gamma_A - (V_{B_i})^{-1} \mathbf{D\Pi D}^T$$
$$= \begin{pmatrix} a - \frac{c^2}{b} & 0 \\ 0 & a \end{pmatrix}, \tag{39}$$

where $\gamma_A = a \cdot \mathbf{I}$, $\mathbf{D} = c \cdot \mathbf{Z}$, $V_{B_i} = b$. And therefore, the symplectic eigenvalue $v_3$ of $\gamma_{(A|B)_i}$ is given by

$$v_3 = \sqrt{a\left(a - \frac{c^2}{b}\right)}. \tag{40}$$

This eigenvalue can be used to calculate the entropy $S_{(A|B)_i}$. Thereby we can obtain the SKR $R_i^\blacktriangleleft$ for RR using homodyne detection.

*C. Analysis of Subchannel Crosstalk*

For multicarrier systems, crosstalk noise is an additional noise compared with single carrier systems, which may occur in neighboring subchannels. It is an inherent characteristic of optical devices which is mainly caused by the imperfection of optical switches, optical filters or other optical elements. As a result, some information called crosstalk information from adjacent channels may leak, thus affecting the security of the system. The crosstalk information $S_{C_i}$ in the $i$-th subchannel can be expressed as [49]

$$S_{C_i} = \sum_{l \neq i} C_l S_{AB_{(l)}} \tag{41}$$

where, $0 \leqslant C_l \leqslant 1$ is the crosstalk coefficient which can be obtained by the actual experimental setup. $S_{AB_{(l)}}$ is the Holevo information between Alice and Bob in the $l$-th subchannel, for all $l \neq i$, given by

$$S_{AB_{(l)}} = S_{B_l} - S_{(B|A)_l}. \tag{42}$$

In order to calculate the value of $S_{AB_{(l)}}$, we know that the covariance matrix $\gamma_{AB_{(l)}}$ can be expressed as

$$\gamma_{AB_{(l)}} = \begin{pmatrix} V_l \cdot \mathbf{I} & \sqrt{T_l(V_l^2 - 1)} \cdot \mathbf{Z} \\ \sqrt{T_l(V_l^2 - 1)} \cdot \mathbf{Z} & [(1-T_l)W_l + T_lV_l] \cdot \mathbf{I} \end{pmatrix}. \tag{43}$$

Therefore, the symplectic eigenvalues of $\gamma_{AB_{(l)}}$ can be calculated by using Eq. (27) and the value of $S_{AB_{(l)}}$ can be obtained.

Since the crosstalk noise in subchannels can act as Gaussian noise to Bob, this additional noise is already included in the subchannel noise $W_i$ of Eve's optimal collective Gaussian attack [49]. The change of Holevo information between Eve and Alice (Bob) caused by crosstalk noise is as follows [49].

$$\tilde{S}_{AE_{(i)}}(\tilde{S}_{BE_{(i)}}) = S_{AE_{(i)}}(S_{BE_{(i)}}) + \sum_{i=0}^{N-1} |T_i|^2 S_{C_i}. \tag{44}$$

As for the influence of crosstalk noise on the security of the system, Theorem 3 of Ref. [49] has proved that under the optimal Gaussian collective attack, any crosstalk between subchannels is not allowed to leak more information to Eve than single-carrier CVQKD protocols. The theorem is as follows.

**Theorem** [49] Under the optimal Gaussian collective attack, suppose $\tilde{\gamma} > 0$ is a non-zero crosstalk between subchannels in a multicarrier quadrature division modulation setup, and $S_{BE_{single}}$ is Eve's Holevo information for single carrier CVQKD. Then, $S_{BE_{\tilde{\gamma}}} \leq S_{BE_{single}}$, where $S_{BE_{\tilde{\gamma}}}$ is Eve's Holevo information for multicarrier quadrature division modulation in the case of crosstalk.

According to the theorem, under the optimal Gaussian collective attack, crosstalk noise does not affect on the security of the multicarrier quadrature division modulation.

TABLE I
FIVE THz WAVE HIGH TRANSMITTANCE WINDOWS

| Number | Frequency (GHz) | Absorption coefficient $\alpha_f$(dB/km) |
|--------|-----------------|------------------------------------------|
| 1 | 300 | 3 |
| 2 | 350 | 7 |
| 3 | 410 | 12 |
| 4 | 670 | 38 |
| 5 | 850 | 51 |

Subsequently, for THz-MCM-CVQKD system, the total SKR $K$ can be derived as a sum of the key rates of each channel

$$K = f_{\rm rep} \sum_{i=0}^{N-1} \left[ \beta I_{AB_{(i)}} - \tilde{S}_{AE_{(i)}}(\tilde{S}_{BE_{(i)}}) \right]$$

$$= f_{\rm rep} \left[ \sum_{i=0}^{N-1} \left( R_i^{\blacktriangleright \text{or} \blacktriangleleft} - |T_i|^2 S_{C_i} \right) \right], \qquad (45)$$

where $f_{\rm rep}$ is the pulse repetition rate.

## IV. SECRET KEY RATE OF THz-MCM-CVQKD

### A. Channel Model Under Indoor Environment

When THz waves travel in the atmosphere, path loss will occur. It mainly consists of miscellaneous loss, atmospheric molecular absorption loss and free space path loss. Under indoor environment, we only consider small miscellaneous loss and atmospheric molecular absorption loss for short distance. The transmittance $T_{AL}$ in the atmosphere can be expressed as

$$T_{AL} = 10^{-\alpha_f d/10}, \qquad (46)$$

where $\alpha_f$ is the atmospheric absorption coefficient at frequency $f$ and $d$ is the transmission distance.

The loss of atmospheric absorption depends on the composition of the mixed gas molecules (i.e. oxygen ($O_2$), water vapor ($H_2O(g)$), carbon dioxide ($CO_2$), nitrogen ($N_2$), etc.) found along the path. We assume that the atmospheric environment is mainly composed of $N_2$ (78%) and $O_2$ (21%) as well as $H_2O(g)$ (1%). Since different gas molecules have extremely different effects on electromagnetic waves of different bands, for THz bands, $O_2$ and $H_2O(g)$ are the most important absorption components. The atmospheric absorption coefficient $\alpha_f$ at frequency $f$ can be given by

$$\alpha_f = \alpha_f(O_2) + \alpha_f(H_2O(g)). \qquad (47)$$

Based on the method described in ITU recommendation P.676-10 [55], we calculate the atmospheric attenuation at wave frequencies from 0.1 THz to 1 THz. The parameters take the typical values, i.e., the water vapor density is $7.53\text{g}/\text{m}^3$ and the atmospheric pressure $P$ is 1013.25hPa. The results also are shown in Fig. 6 in which we can obtain that water vapor in the atmosphere plays a major role in the attenuation of THz waves. We can also see that there are some spectral windows with low absorption attenuation and the transmittance can reach almost 100%. Most of the former works have been performed within these spectral windows [31], [56], [57]. We select five main available centre frequencies shown in Table I. Table II shows the parameters setting.

### B. Simulation and Discussion Under Indoor Environment

Numerical simulations between the SKR and the transmission distance for the THz-MCM-CVQKD under indoor environment is shown in Fig. 7. For a given subcarriers number $N = 1, 4, 8, 16, 32$, we assume that each subchannel is the same, the pulse repetition rate as $f_{\rm rep} = 1$ MHz, the modulation variance as $V_{\rm mod} = 100$, the frequency of subcarriers as $f = 300$ GHz, corresponding atmospheric absorption coefficient as $\alpha_f = 3$ dB/km and the absolute temperature as $\tau = 300$ K (room temperature). Obviously, as the number of the subcarriers $N$ increases, the SKR increases significantly in DR and RR. However, the maximal transmission distance decreases with the increase of $N$. This is because the crosstalk noise of subchannels increases with the increase of $N$. The maximal transmission distance of 32 subcarriers is 24 m in DR and 0.44 m in RR which is slightly shorter than that of single carrier (28 m in DR and 0.45 m in RR), but the SKR is significantly increased.

In Fig. 8, we plot the SKR of THz-MCM-CVQKD system with different frequencies ($f = 300, 410, 670$ GHz). Different frequencies have influence on the SKR and maximal transmission distance. As the frequency $f$ increases, although the shot noise decreases, the atmospheric absorption coefficient increases and the final result is that the SKR and the transmission distance decrease in DR and RR. The maximal distance of 32 subcarriers with 410 GHz and 670 GHz is nearly 8 m and 4.8 m respectively in DR and is 0.21 m and 0.18 m in RR.

In addition, we also consider the influence of channel noise on the system shown in Fig. 9(a). We compare the SKR with single carrier and 32 subcarriers under different channel noise, where the channel noise is 1, 10 and 50 SNU respectively. As depicted in Fig. 9, as the channel noise increases, the secure transmission distance of 32 subcarriers with 300 Ghz decreases from nearly 24 m to 10.5 m in DR.

Next, we will show the improvement of the SKR of THz-MCM-CVQKD system. We describe the increment by defining the multi-channel gain $G$, which can be expressed as

$$G = \frac{K}{R_{\rm single}} = \frac{f_{\rm rep}}{R_{\rm single}} \left[ \sum_{i=0}^{N-1} \left( R_i^{\blacktriangleright \text{or} \blacktriangleleft} - |T_i|^2 S_{C_i} \right) \right], \quad (48)$$

where, $R_{\rm single}$ is the SKR in the single channel CV-QKD and the parameter values are the same as in the multi-channel system. As shown in Fig. 9(b), with the increase of $d$ and $N$, the multi-channel gain $G$ decreases rapidly. When the maximal transmission distance is reached, $G$ drops to 0. We find that in the case of short distance (e.g., $d \leqslant 4$ m), the gain of THz-MCM-CVQKD system is approximately $N$ times than the single carrier. Therefore, the SKR is greatly improved.

The above results show that THz waves have potential application prospects in wireless short distance high-speed quantum communication under indoor enviroment. Lower THz frequencies and increasing the number of subcarriers in DR or RR can achieve optimal performance. In this case, DR has higher noise immunity than RR.

TABLE II
PARAMETER SETTING. INDOOR ENVIRONMENT AND INTER-SATELLITES LINK

| Symbol | Parameter setting | Indoor environment | Inter-satellites link |
|---|---|---|---|
| $V_S$ | Shot noise | Independent variable | Independent variable |
| $T$ | Transmittance | Independent variable | Independent variable |
| $f$ | Frequency | Independent variable | Independent variable |
| $W$ | Channel noise | Independent variable | Independent variable |
| $\varepsilon$ | Excess noise | – | 0.05 |
| $\eta$ | Detection efficiency | 1 | 0.7 |
| $\beta$ | Reconciliation efficiency | 1 | 0.98 [58] |
| $V_{\text{mod}}$ | Modulation variance | 100 | 10 |
| $\tau$ | Temperature | 300 K | 30 K |
| $f_{\text{rep}}$ | Pulse repetition rate | 1 MHz | 1 MHz |
| $z_0$ | Beam-waist radius | – | 20 cm |
| $l_a$ | Receiver-aperture radius | – | 20 cm |
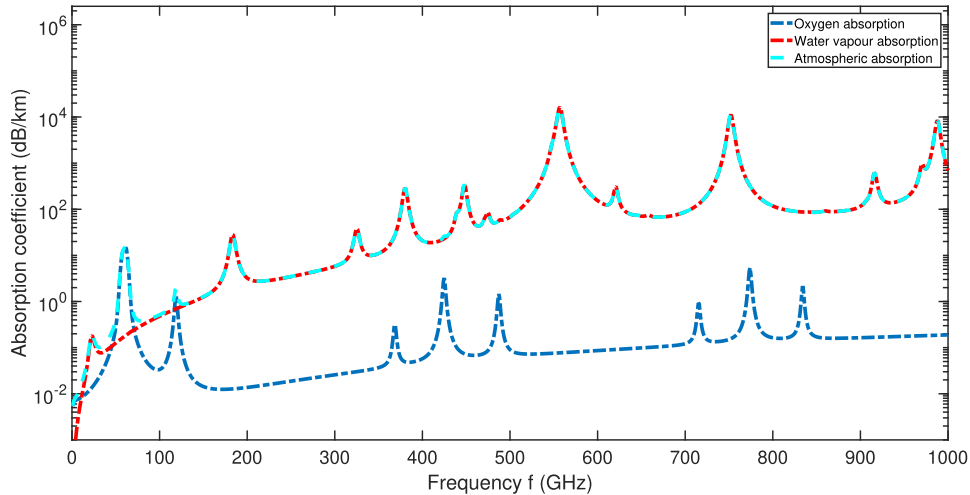


Fig. 6.   Oxygen absorption coefficient, water vapour absorption coefficient and atmospheric absorption coefficient in the frequency range of 0.1 THz - 1 THz. (Blue) Oxygen absorption. (Red) Water vapour absorption. (Light blue) Atmospheric absorption.

## C.  Channel Model in Inter-Satellite Links

When electromagnetic waves propagate in free space channels, it will suffer from absorption, scattering and turbulence, etc. The atmospheric turbulence can cause beam drift and scintillation effects, leading to degradation and severe fading of quantum entanglement. Satellite-based QKD usually involves the exchange of information through atmospheric channels. The atmosphere effect limits the transmission performance of THz waves. However, THz QKD will have potential applications in secure inter-satellite communications. In this case, the absorption is almost negligible, and the beam drift effect can be ignored, which allows us to approximately attribute the channel to a fixed attenuation with only diffraction effects. The loss derived from diffraction effects is caused only by the size of the diffracted beam at the receiving aperture. The transmittance $T_{SL}$ can be given by [32]

$$T_{SL} = 1 - \exp(-2l_a^2/z^2(d)), \qquad (49)$$

where $l_a$ denotes the radius of receiving aperture, $d$ denotes the path distance of the beam and $z(d)$ denotes the beam radius at distance $d$. Using the Gaussian approximation, $z(d)$ is given

by [32]

$$z(d) = z_0\sqrt{1 + (\lambda d/\pi z_0^2)^2}, \qquad (50)$$

where $z_0$ denotes the radius of the waist of the beam and $\lambda$ denotes the wavelength of the beam. Noted that the waist of the beam and receiving aperture are affected by the limitations of the actual hardware. In this model, we assume that temperature of the environment is 30 K because a recent thermal analysis of space-based quantum experiments has shown that the satellite-board optical bench can be cooled down to 27 K [59]. The parameters setting is shown in Table II.

## D.  Simulation and Discussion in Inter-Satellite Links

In inter-satellite links, we plot the relationship between the SKR and the transmission distance in DR and RR, as shown in Fig. 10. Here we let the modulation variance $V_{\text{mod}} = 10$, the detection efficiency $\eta = 0.7$, the frequency of subcarriers $f = 10$ THz, the pulse repetition rate $f_{\text{rep}} = 1$ MHz, the absolute temperature $\tau = 30\ K$, and the number of sucarriers $N = 1, 4, 8, 16, 32$ respectively. Similarly, as the increase of $N$, the SKR increases significantly. Numerical simulations show that the maximal transmission distance of 32 subcarriers is
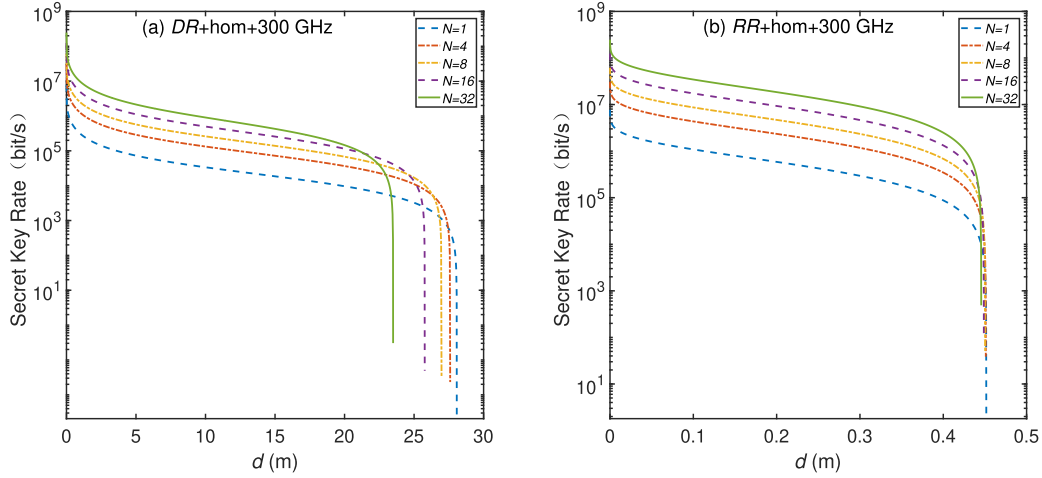
Fig. 7. The SKR of THz-MCM-CVQKD as a function of the transmission distance using homodyne detection under indoor environment in DR for (a) and in RR for (b). The subcarriers number as $N = 1, 4, 8, 16, 32$, the modulation variance as $V_{\mathrm{mod}} = 100$, The frequency of the subcarriers as $f = 300$ GHz, corresponding atmospheric absorption coefficient as $\alpha_f = 3$ dB/km and the absolute temperature as $\tau = 300$ K.
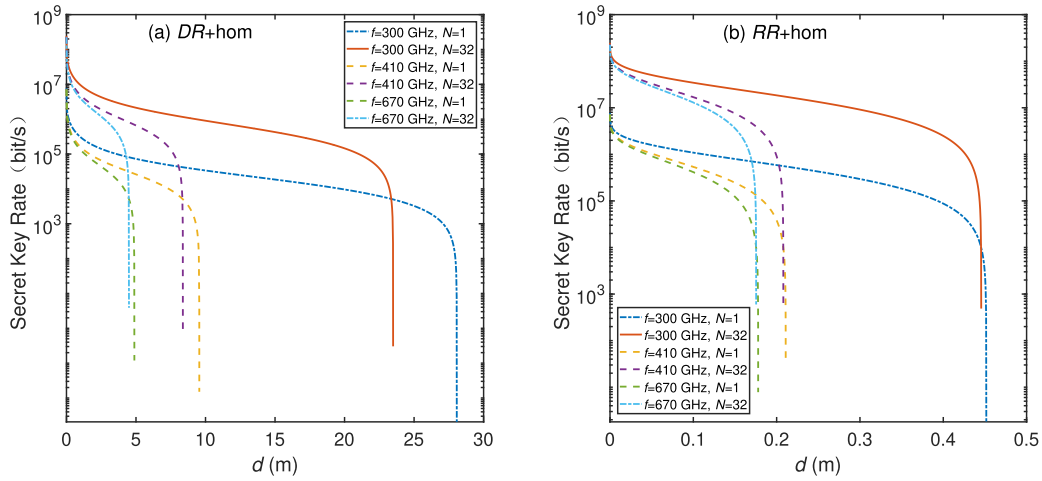


Fig. 8. The SKR of THz-MCM-CVQKD system with different frequency under indoor environment in DR for (a) and in RR for (b). The frequency of the subcarries as $f = 300, 410, 670$ GHz and the subcarriers number as $N = 1, 32$, respectively.
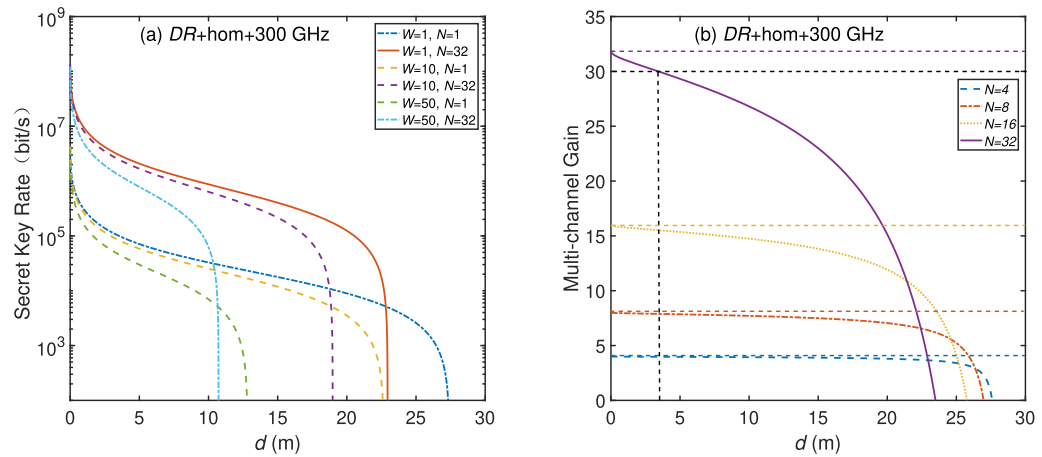


Fig. 9. (a) Effects of different channel noise on THz-MCM-CVQKD system under indoor environment with $f = 300$ GHz in DR. The channel noise is 1, 10 and 50 SNU respectively. (b) The relation between the multi-channel gain $G$ and the transmission distance $d$ with $f = 300$ GHz in DR.
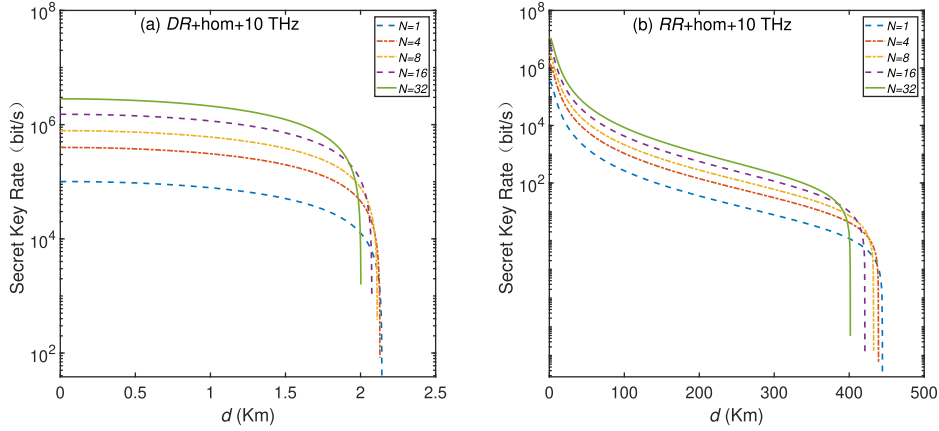
Fig. 10. The SKR of THz-MCM-CVQKD in inter-satellite links in DR for (a) and in RR for (b). The modulation variance as $V_{\mathrm{mod}} = 10$, the detection efficiency $\eta$ as 0.7, the pulse repetition rate as $f_{\mathrm{rep}} = 1$ MHz, the frequency of the subcarrier as $f = 10$ THz, the absolute temperature as $\tau = 30$ K, and the number of subcarriers as $N = 1, 4, 8, 16, 32$ respectively.
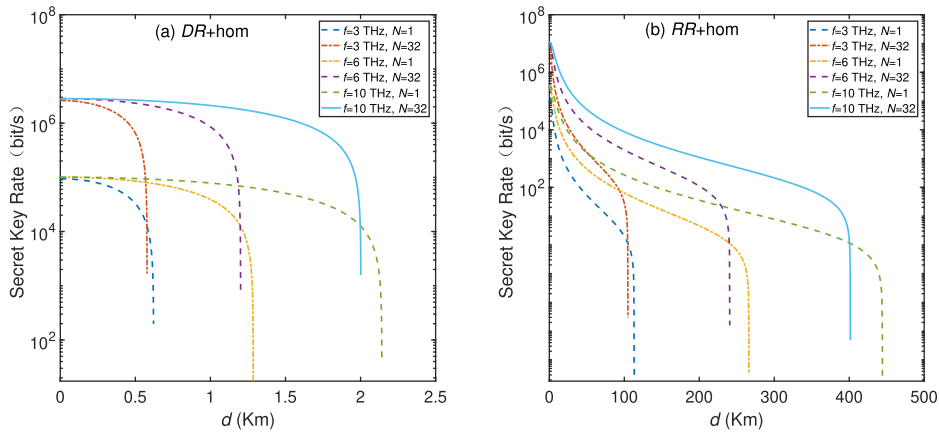


Fig. 11. The SKR of THz-MCM-CVQKD system with different frequency in inter-satellite links in DR for (a) and in RR for (b). The modulation variance as $V_{\mathrm{mod}} = 10$, the detection efficiency as $\eta = 0.7$, the pulse repetition rate as $f_{\mathrm{rep}} = 1$ MHz, the frequencies of the subcarrieres as $f = 3, 6, 10$ THz, the absolute temperature as $\tau = 30$ K, and the number of subcarriers as $N = 1, 32$ respectively.

nearly 2 km in DR while it can exceed 400 km in RR. This is because DR has a 3 dB limit, that is, when the channel loss is greater than 3 dB, the CV-QKD protocols will can not generate the secure keys. Interestingly, we find that a RR-based SKR of $10^3$ bit/s can attain 100 km and 200 km transmission distance when the number of subcarriers is more than 4 and 16, respectively. It is also observed that when the number of subcarriers is 32, a $10^2$ bit/s RR-based SKR can be achieved at 10 THz frequency in a nearly 400 km inter-satellite link. Moreover, as the number of subcarriers increases, the SKR will continue to increase. The results indicate that THz-MCM-CVQKD of long distance with high SKR can be achieved in the inter-satellite link.

In Fig. 11, we analyse the influence of different frequencies ($f = 3, 6, 10$ THz) on the THz-MCM-CVQKD system. we find that as the frequency $f$ increases, the noise immunity increases significantly in DR and RR. The maximal transmission distance of 32 subcarriers with 3 THz and 6 THz is nearly 0.55 km and 1.2 km respectively in DR. We can also observe that a $10^2$ bit/s

RR-based SKR can be achieved over a 100 km 3 THz and a 200 km 6 THz inter-satellite link respectively. The results shown here again support the feasibility of inter-satellite THz-MCM-CVQKD.

We also demonstrate the improvement of the SKR of THz-MCM-CVQKD system by using Eq. (48) in inter-satellite links. Fig. 12 shows the relation between multi-channel gain $G$ and $d$ in inter-satellite links in RR. Similarly, with the increase of $d$ and $N$, the multi-channel gain $G$ decreases rapidly. For $d \leqslant 250$ km, the system greatly improves the SKR with a approximately $N$ times gain. That is to say, THz-MCM-CVQKD system can provide an efficient path for high-speed quantum communication in inter-satellite links.

From our analysis, the proposed system can achieve the optimal performance in inter-satellite links with higher THz frequency and increasing the number of subcarriers. In this case, the advantage of using RR is obvious, which is also the reconciliation method of post-processing adopted by most current CVQKD protocols.
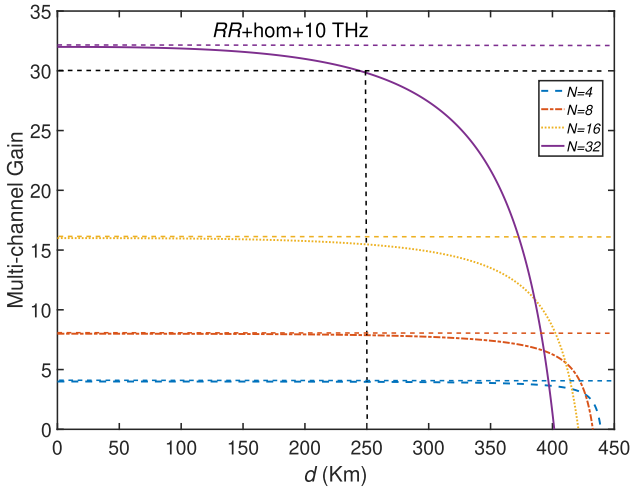
Fig. 12. The relation between the multi-channel gain $G$ and the transmission distance $d$ in RR. The frequency of the subcarriers as $f = 10$ THz.
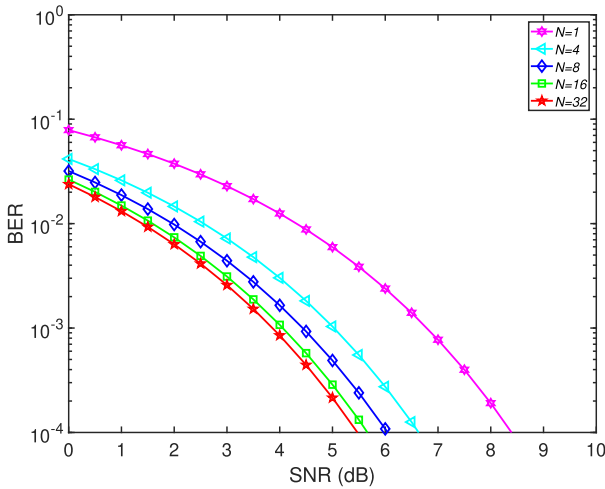


Fig. 13. The BER performance in the system under different SNR when $N = 1, 4, 8, 16, 32$.

Since the transmitted pulses can be changed by distortion, interference and noise, we finally analyze the bit error rate (BER) performance in the system under different SNR when $N = 1, 4, 8, 16, 32$. The BER is defined as the ratio of error bits to total transmission bits. The asymptotic BER can be calculated by [60]

$$\mathrm{BER} = \frac{\sqrt{M} - 1}{\sqrt{M} \log_2 \sqrt{M}} \mathrm{Q} \left( \sqrt{\frac{2^{\sqrt{N}} - 1}{2^{\sqrt{N}-1}} \frac{3\mathrm{SNR} \log_2 M}{2(M-1)}} \right) \tag{51}$$

where,

$$\mathrm{Q}(x) = \int_x^\infty \frac{2}{\sqrt{\pi}} e^{-u^2} du, \tag{52}$$

$M$ denotes the modulation level (we employ $M = 4$ in the system). As shown in Fig. 13, we can observe that compared with a single carrier, as the number of subcarriers increases, the

required SNR decreases for the same BER. The required SNR for a BER of $10^{-4}$ is about 8.3 dB, 6.6 dB, 6 dB, 5.6 dB and 5.4 dB, respectively when $N = 1, 4, 8, 16, 32$. For SNR=2 dB, as the number of subcarriers increases from 1 to 32, the BER decreases from $3.75 \times 10^{-2}$ to $6.3 \times 10^{-3}$. Thus, an efficient post-processing is essential in the protocol.

### E. Comparisons

In this section, we will compare the performance of our scheme with the schemes in Ref. [26], [27], [32]. In order to facilitate comparison, in both indoor environment or inter-satellite links, we set the same parameter values as the schemes in the above references. Under indoor environment, we set $f = 300$ GHz, $\eta = 0.1$, $\tau = 300$ K, $\beta = 1$, $\varepsilon = 0.01$, $V_{\mathrm{mod}} = 100$, $f_{\mathrm{rep}} = 1$ MHz respectively and compare the SKR and the gain with Ref. [26], [27] in DR. In inter-satellite links, we set $f = 10$ THz, $\eta = 0.1$, $\tau = 30$ K, $\beta = 0.98$, $\varepsilon = 0.01$, $V_{\mathrm{mod}} = 10$, $z_0 = 10$ cm, $l_a = 10$ cm, $f_{\mathrm{rep}} = 1$ MHz respectively and also compare the SKR and the gain with Ref. [32] in RR.

We compare the SKR of THz-MCM-CVQKD with Ref. [26], [27] under indoor environment as shown in Fig. 14(a). We can see that for a single carrier system, the maximal transmission distance of Ref. [26] is about 2.4 m, that of Ref. [27] is about 1.9 m and that of THz-MCM-CVQKD is about 2.5 m ($N = 1$). For $d \geqslant 1.5$ m, the noise immunity of Ref. [26] and THz-MCM-CVQKD ($N = 1$) is higher than Ref. [27]. At the same distance, the SKR of THz-MCM-CVQKD ($N = 1$) is higher than that of Ref. [26], [27]. For $N > 1$, THz-MCM-CVQKD has an obvious advantage in improving SKR. In particular, for $N = 32$, the SKR of THz-MCM-CVQKD is much higher than that of Ref. [26], but their maximal transmission distances are almost the same. The comparison of the SKR of THz-MCM-CVQKD with Ref. [32] in inter-satellite links as shown in Fig. 14(b). The maximal transmission distance of both Ref. [32] and THz-MCM-CVQKD exceeds 120 km. For a single carrier system, the SKR of THz-MCM-CVQKD ($N = 1$) is slightly higher than that of Ref. [32] at the same distance. This might be correlated to the estimation formula of SKR. However, for $N > 1$, THz-MCM-CVQKD has powerful advantages in improving the SKR compared with Ref. [32].

In Fig. 15(a), we also compare the gain of THz-MCM-CVQKD with Ref. [26], [27] under indoor environment. We can obtain that for $d > 1.5$ m, the gain of Ref. [26], [27] is gradually lower than that of THz-MCM-CVQKD ($N = 1$) and finally drops to 0 when they reach the maximal transmission distance. For $d \leqslant 1.5$ m, the gain of THz-MCM-CVQKD ($N > 1$) is approximately $N$ times than that of Ref. [26], [27]. As shown in Fig. 15(b), for $d \leqslant 120$ km, the gain of THz-MCM-CVQKD ($N = 1$) and Ref. [32] is almost the same in inter-satellite links. For $N > 1$ and $d \leqslant 120$ km, THz-MCM-CVQKD also greatly improves the SKR with a approximately $N$ times gain than that of Ref. [32]. In short, the above results show that THz-MCM-CVQKD system has powerful advantages in improving the SKR and the gain of the system is approximately $N$ times as many as the one of other systems within a certain range of transmission distance.
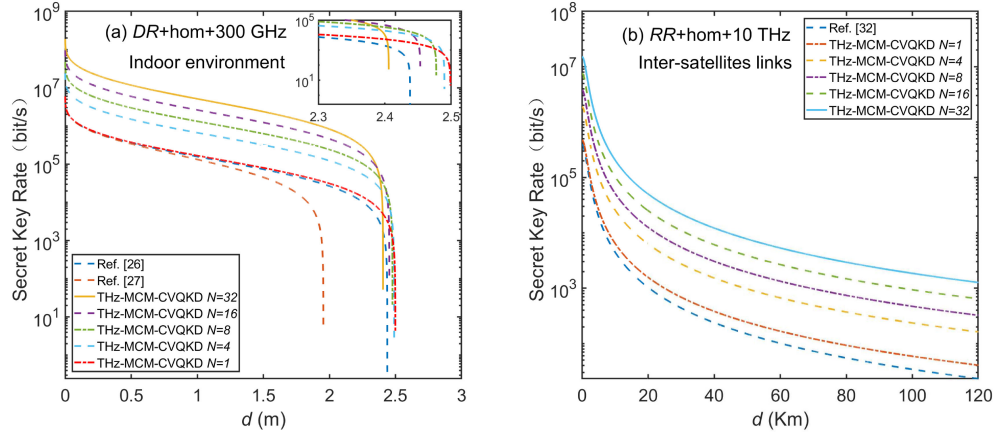
Fig. 14. Comparisons of the SKR of THz-MCM-CVQKD with Ref. [26], [27] under indoor environment for (a) and Ref. [32] in inter-satellite links for (b).
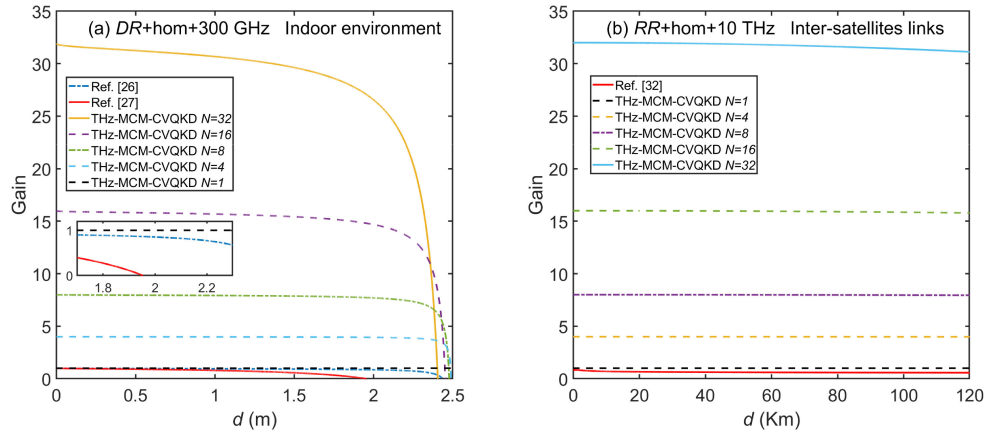


Fig. 15. Comparisons of the gain of THz-MCM-CVQKD with Ref. [26], [27] under indoor environment for (a) and Ref. [32] in inter-satellite links for (b).

## V. CONCLUSION

We evaluate the performance of THz-MCM-CVQKD and show that the MCM technology is very effective for improving the SKR at the cost of slightly shortening the maximal transmission distance. Under indoor environment, the proposed system has great development potential in wireless short-range secure and high-speed communication. In inter-satellite links, we observe that THz-MCM-CVQKD at 10 THz frequency with 32 subcarriers can work in a secure distance of more than 400 km. The results strongly support the feasibility of inter-satellite THz-MCM-CVQKD. Moreover, with the increase of the number of subcarriers, the SKR will continue to increase. Therefore, THz-MCM-CVQKD can provide an efficient path to build a secure and high-speed global quantum communication network. However, for THz-QKD systems, the secure transmission distance depends mainly on the channel noise and antenna gain. In the process of practical application, various technologies need to be combined, e.g., noise suppression, high gain antenna, high efficiency detector, and accurate parameter estimation algorithm, etc. These are what we need to overcome in the future.

## REFERENCES

[1] F. Grosshans and P. Grangier, "Continuous variable quantum cryptography using coherent states," *Phys. Rev. Lett.*, vol. 88, no. 5, 2002, Art. no. 057902.

[2] F. Grosshans, A. G. Van, J. Wenger, R. Brouri, N. J. Cerf, and P. Grangier, "Quantum key distribution using Gaussian-modulated coherent states," *Nature*, vol. 421, pp. 238–241, 2003.

[3] V. Scarani, H. Bechmannpasquinucci, N. J. Cerf, M. Dusek, N. Lutkenhaus, and M. Peev, "The security of practical quantum key distribution," *Rev. Mod. Phys.*, vol. 81, no. 3, pp. 1301–1350, 2009.

[4] C. Weedbrook *et al.*, "Gaussian quantum information," *Rev. Mod. Phys.*, vol. 84, no. 2, pp. 621–669, 2011.

[5] C. Weedbrook, S. Pirandola, and T. C. Ralph, "Continuous-variable quantum key distribution using thermal states," *Phys. Rev. A*, vol. 86, no. 2, 2012, Art. no. 022318.

[6] F. Laudenbach *et al.*, "Continuous-variable quantum key distribution with Gaussian modulation-the theory of practical implementations," *Adcanced Quantum Technol.*, vol. 1, no. 1, 2018, Art. no. 1800011.

[7] S. Pirandola, U. L. Andersen, L. Banchi, M. Berta, and P. Wallden, "Advances in quantum cryptography," *Adv. Opt. Photon.*, vol. 12, pp. 1012–1236, 2020.

[8] L. Gyongyosi, L. Bacsardi, and S. Imre, "A survey on quantum key distribution," *Infocom. J.*, vol. 11, no. 2, pp. 14–21, 2019.

[9] C. H. Bennett and G. Brassard, "Quantum cryptography: Public key distribution and coin tossing," in *Proc. IEEE Int. Conf. Comput., Syst. Signal Process.*, 1984, pp. 175–179.

[10] C. H. Bennett, "Quantum cryptography using any two nonorthogonal states," *Phys. Rev. Lett.*, vol. 68, no. 21, pp. 3121–3124, 1992.

[11] S. Pirandola, R. Garcia-Patron, S. L. Braunstein, and S. Lloyd, "Direct and reverse secret-key capacities of a quantum channel," *Phys. Rev. Lett.*, vol. 102, no. 5, 2009, Art. no. 050503.

[12] S. Pirandola, A. Serafini, and S. Lloyd, "Correlation matrices of two-mode bosonic systems," *Phys. Rev. A*, vol. 79, no. 5, pp. 1744–1747, 2009.

[13] C. Weedbrook, S. Pirandola, S. Lloyd, and T. C. Ralph, "Quantum cryptography approaching the classical limit," *Phys. Rev. Lett.*, vol. 105, no. 11, 2010, Art. no. 110501.

[14] N. Hosseinidehaj, Z. Babar, R. Malaney, S. X. Ng, and L. Hanzo, "Satellite-based continuous-variable quantum communications: State-of-the-art and a predictive outlook," *IEEE Commun. Surv. Tut.*, vol. 21, no. 1, pp. 881–919, Jan.–Mar. 2019.

[15] D. Elser, T. J. Bartley, B. Heim, C. Wittmann, D. Sych, and G. Leuchs, "Feasibility of free space quantum key distribution with coherent polarization states," *New J. Phys.*, vol. 11, no. 4, 2009, Art. no. 045014.

[16] Z. Qu and I. B. Djordjevic, "Four-dimensionally multiplexed eight-state continuous-variable quantum key distribution over turbulent channels," *IEEE Photon. J.*, vol. 9, no. 6, Dec. 2017, Art. no. 7600408.

[17] O. Elmabrok and M. Razavi, "Feasibility of wireless quantum key distribution in indoor environments," in *Proc. IEEE Globecom Workshops*, 2015, pp. 1–2.

[18] J. Lodewyck *et al.*, "Quantum key distribution over 25 km with an all-fiber continuous-variable system," *Phys. Rev. A*, vol. 76, no. 4, pp. 538–538, 2007.

[19] O. Elmabrok and M. Razavi, "Wireless quantum key distribution in indoor environments," *J. Opt. Soc. Amer. B*, vol. 35, no. 2, pp. 197–207, 2018.

[20] P. Jouguet, S. Kunzjacques, A. Leverrier, P. Grangier, and E. Diamanti, "Experimental demonstration of long-distance continuous-variable quantum key distribution," *Nature Photon.*, vol. 7, no. 5, pp. 378–381, 2013.

[21] B. Qi, L. Huang, L. Qian, and H. Lo, "Experimental study on the Gaussian-modulated coherent-state quantum key distribution over standard telecommunication fibers," *Phys. Rev. A*, vol. 76, no. 5, 2007, Art. no. 052323.

[22] S. Fossier, E. Diamanti, T. Debuisschert, A. Villing, R. Tuallebrouri, and P. Grangier, "Field test of a continuous-variable quantum key distribution prototype," *New J. Phys.*, vol. 11, no. 4, 2009, Art. no. 045023.

[23] R. García-Patrón and N. J. Cerf, "Unconditional optimality of Gaussian attacks against continuous-variable quantum key distribution," *Phys. Rev. Lett.*, vol. 97, no. 19, 2006, Art. no. 190503.

[24] M. Navascués, F. Grosshans, and A. Acín, "Optimality of Gaussian attacks in continuous variable quantum cryptography," *Phys. Rev. Lett.*, vol. 97, no. 19, 2006, Art. no. 190502.

[25] F. Furrer *et al.*, "Continuous variable quantum key distribution: Finite-key analysis of composable security against coherent attacks," *Phys. Rev. Lett.*, vol. 109, no. 10, 2012, Art. no. 100502.

[26] C. Ottaviani *et al.*, "Terahertz quantum cryptography," *IEEE J. Sel. Areas Commun.*, vol. 38, no. 3, pp. 483–495, Mar. 2020.

[27] X. Liu, C. Zhu, N. Chen, and C. Pei, "Practical aspects of terahertz wireless quantum key distribution in indoor environments," *Quantum Inf. Process.*, vol. 17, no. 11, 2018, Art. no. 304.

[28] V. Petrov, A. Pyattaev, D. Moltchanov, and Y. Koucheryavy, "Terahertz band communications: Applications, research challenges, and standardization activities," in *Proc. 8th Int. Congr. Ultra Modern Telecommun. Control Syst. Workshops*, 2016, pp. 183-190.

[29] Y. Q. He, Y. Mao, H. Zhong, D. Huang, and Y. Guo, "Hybrid linear amplifier-involved detection for continuous variable quantum key distribution with thermal states," *Chin. Phys. B*, vol. 29, no. 5, 2020, Art. no. 050309.

[30] X. Yu *et al.*, "160 Gbit/s photonics wireless transmission in the 300-500 GHz band," *Apl Photon.*, vol. 1, 2016, Art. no. 081301.

[31] F. Sheikh, N. Zarifeh, and T. Kaiser, "Terahertz band: Channel modelling for short-range wireless communications in the spectral windows," *IET Microw. Antennas Propag.*, vol. 10, no. 13, pp. 1435–1444, 2016.

[32] Z. Wang, R. Malaney, and J. Green, "Inter-satellite quantum key distribution at terahertz frequencies," in *Proc. ICC IEEE Int. Conf. Commun.*, 2019, pp. 1-7.

[33] C. K. Walker and C. A. Kulesa, "Terahertz astronomy from the coldest place on earth," in *Proc. Joint 30th Int. Conf. Infrared Millimeter Waves & 13th Int. Conf. Terahertz Electron.*, 2005, vol. 1, pp. 3-4.

[34] H. Yang *et al.*, "Exceptional terahertz transparency and stability above dome a, antarctica," *Publ. Astron. Soc. Pac.*, vol. 122, no. 890, pp. 490–494, 2010.

[35] J. Ma *et al.*, "Security and eavesdropping in terahertz wireless links," *Nature*, vol. 563, pp. 89–93, 2018.

[36] A. J. Seeds, H. Shams, M. J. Fice, and C. C. Renaud, "Terahertz photonics for wireless communications," *J. Lightw. Technol.*, vol. 33, no. 3, pp. 579–587, 2015.

[37] M. J. Rosker and H. B. Wallace, "Imaging through the atmosphere at terahertz frequencies," in *Proc. IEEE/MTT-S Int. Microw. Symp.*, 2007, pp. 773-776.

[38] A. Ortigosa-Blanch and J. Capmany, "Subcarrier multiplexing optical quantum key distribution," *Phys. Rev. A*, vol. 73, no. 2, 2006, Art. no. 024305.

[39] J. Fang, P. Huang, and G. H. Zeng, "Multichannel parallel continuous-variable quantum key distribution with Gaussian modulation," *Phys. Rev. A*, vol. 89, no. 2, 2014, Art. no. 022315.

[40] H. Zhang, M. Yu, D. Huang, J. Li, L. Zhang, and Y. Guo, "Security analysis of orthogonal-frequency-division-multiplexing-based continuous-variable quantum key distribution with imperfect modulation," *Phys. Rev. A*, vol. 97, no. 5, 2018, Art. no. 052328.

[41] W. Zhao, Q. Liao, D. Huang, and Y. Guo, "Performance analysis of the satellite-to-ground continuous-variable quantum key distribution with orthogonal frequency division multiplexed modulation," *Quantum Inf. Process.*, vol. 18, no. 1, 2019, Art. no. 39.

[42] L. Gyongyosi and S. Imre, "Low-dimensional reconciliation for continuous-variable quantum key distribution," *Appl. Sci.*, vol. 8, no. 1, 2013, Art. no. 87.

[43] L. Gyongyosi, "Singular value decomposition assisted multicarrier continuous-variable quantum key distribution," *Theor. Comput. Sci.*, vol. 801, pp. 35–63, 2020.

[44] L. Gyongyosi and S. Imre, "Multiple access multicarrier continuous-variable quantum key distribution," *Chaos Soliton. Fract.*, vol. 114, pp. 491–505, 2018.

[45] L. Gyongyosi, S. Imre, and H. V. Nguyen, "A survey on quantum channel capacities," *IEEE Commun. Surv. Tut.*, vol. 20, no. 2, pp. 1149–1205, Apr.–Jun. 2018.

[46] L. Gyongyosi and S. Imre, "Secret key rate proof of multicarrier continuous-variable quantum key distribution," *Int. J. Commun. Syst.*, vol. 32, no. 4, 2019, Art. no. e3865.

[47] J. Capmany, A. Ortigosa-Blanch, J. Mora, A. Ruiz-Alba, W. Amaya, and A. Martinez, "Analysis of subcarrier multiplexed quantum key distribution systems: Signal, intermodulation, and quantum bit error rate," *IEEE J. Sel. Top. Quantum Electron.*, vol. 15, no. 6, pp. 1607–1621, Nov./Dec. 2009.

[48] S. Bahrani, M. Razavi, and J. A. Salehi, "Orthogonal frequency-division multiplexed quantum key distribution," *J. Lightw. Technol.*, vol. 33, no. 23, pp. 4687–4698, 2015.

[49] L. Gyongyosi, "Multicarrier continuous-variable quantum key distribution," *Theor. Comput. Sci.*, vol. 816, pp. 67–95, 2020.

[50] D. Hillerkuss *et al.*, "Simple all-optical FFT scheme enabling tbit/s real-time signal processing," *Opt. Exp.*, vol. 18, no. 9, pp. 9324–9340, 2010.

[51] D. Hillerkuss *et al.*, "26 tbit/s line-rate super-channel transmission utilizing all-optical fast fourier transform processing," *Nature Photon.*, vol. 5, no. 6, pp. 364–371, 2011.

[52] J. Schroder, L. B. Du, J. Carpenter, B. J. Eggleton, and A. J. Lowery, "All-optical OFDM with cyclic prefix insertion using flexible wavelength selective switch optical processing," *J. Lightw. Technol.*, vol. 32, no. 4, pp. 752–759, 2014.

[53] Z. Wang, K. Kravtsov, Y. K. Huang, and P. R. Prucnal, "Optical FFT/IFFT circuit realization using arrayed waveguide gratings and the applications in all-optical ofdm system," *Opt. Exp.*, vol. 19, no. 5, pp. 4501–4512, 2011.

[54] G. Scalari, J. Faist, and N. Picque, "On-chip mid-infrared and THz frequency combs for spectroscopy," *Appl. Phys. Lett.*, vol. 114, no. 15, 2019, Art. no. 150401.

[55] Attenuation by atmospheric gases, Rec. ITU-R P.676-10, Int. Telecommun. Union, Geneva, Switzerland, Sept. 2013.

[56] T. Schneider, A. Wiatrek, S. Preussler, M. Grigat, and R. Braun, "Link budget analysis for terahertz fixed wireless links," *IEEE Trans. Terahertz Sci. Technol.*, vol. 2, no. 2, pp. 250–256, Mar. 2012.

[57] R. Piesiewicz *et al.*, "Short-range ultra-broadband terahertz communications: Concepts and perspectives," *IEEE Antennas Propag. Mag.*, vol. 49, no. 6, pp. 24–39, Dec. 2007.

[58] M. Milicevic, C. Feng, L. M. Zhang, and P. G. Gulak, "Key reconciliation with low-density parity-check codes for long-distance quantum cryptography," *EPJ Quantum Technol.*, vol. 4, 2017, Art. no. 1.

[59] G. Hechenblaikner *et al.*, "How cold can you get in space? Quantum Physics at cryogenic temperatures in space," *New J. Phys.*, vol. 16, 2014, Art. no. 013058.

[60] J. van Wyk and L. Linde, "Bit error probability for a M-ary QAM OFDM-based system," in *Proc. AFRICON*, 2007, pp. 1–5.